Research Square

Preprints are preliminary reports that have not undergone peer review.
They should not be considered conclusive, used to inform clinical practice,
or referenced by the media as validated information.

Metal-composition-regulated Au-based nanozymes for enzyme-cascade colorimetric determination of uric acid and sarcosine

Qiu Mao
Chongqing Medical University
Lin He
Chongqing Medical University
Huajia Xu
Chongqing Medical University
Mingmeng Xie
Chongqing Medical University
Siqiao Li
Chongqing Medical University
Shudong Cao
Mudanjiang Maternal and Child Health Hospital
Dan He
Chongqing College of Traditional Chinese Medicine
Zhengwei Zhang
zzwcpu@yeah.net

Chongqing Medical University

Research Article

Keywords: Metal-composition engineering, Protamine functionalization, Enzyme–nanozyme cascade, Colorimetric biosensing, Uric acid and sarcosine

Posted Date: November 26th, 2026

DOI: https://doi.org/10.21203/rs.3.rs-11735880/v1

License: This work is licensed under a Creative Commons Attribution 4.0 International License.
Read Full License

Additional Declarations: No competing interests reported.

Abstract

Rational regulation of nanozyme catalytic preference is essential for developing sensitive and adaptable colorimetric biosensors. Here, we developed a metal-composition-regulated nanozyme platform (Au@Ru/Pt/PRTM) integrating multimetallic catalysis with protamine (PRTM)-mediated biomimetic functionalization for the determination of uric acid (UA) and sarcosine (SA). By incorporating different metal species (Ru, Pd, and Ir) into Au-based nanozymes, distinct peroxidase (POD)- and oxidase (OXD)-like catalytic profiles were achieved, demonstrating the influence of metal composition on catalytic preference. The arginine-rich PRTM provided a biomimetic interfacial environment, while the optimized Au@Ru/Pt/PRTM nanozyme exhibited pronounced POD-like activity and favorable catalytic kinetics. By coupling the nanozyme with urate oxidase and sarcosine oxidase, enzyme–nanozyme cascade colorimetric biosensors were established for UA and SA detection, achieving limits of detection of 0.0927 and 0.75 μM, respectively. The assays demonstrated satisfactory selectivity, resistance to interference, and analytical recoveries in spiked artificial urine samples. This work highlights metal-composition engineering combined with biomimetic interfacial functionalization as a promising strategy for tailoring nanozyme catalytic behavior and developing sensitive colorimetric biosensors for biochemical analysis.

Introduction

Accurate determination of disease-associated metabolites is essential for clinical biochemical analysis and metabolic health assessment. Uric acid (UA), the final product of purine metabolism in humans, is closely associated with hyperuricemia, gout, and chronic kidney disease, making its quantitative determination important for metabolic and renal health assessment [1–3]. Sarcosine (SA), an intermediate in glycine and creatine metabolism, has also attracted considerable attention as a potential prostate cancer-associated metabolite [4–6]. Although chromatographic and mass spectrometric methods provide reliable analytical performance, their dependence on sophisticated instrumentation, specialized personnel, and relatively complex procedures can limit their applicability in decentralized testing [7–9]. Consequently, developing simple, sensitive, and cost-effective biosensing strategies for UA and SA determination remains of considerable interest in biochemical analysis and health monitoring.

Nanozymes, a class of nanomaterials with intrinsic enzyme-mimicking catalytic activities, have emerged as promising catalytic signal transducers for biosensing owing to their structural tunability, operational stability, and ease of functionalization [10–12]. Among their diverse catalytic functions, peroxidase (POD)- and oxidase (OXD)-like activities are particularly attractive for colorimetric analysis because they enable the oxidation of chromogenic substrates through H_2O_2-dependent and molecular oxygen-mediated pathways, respectively [13]. These catalytic pathways provide opportunities to construct different sensing configurations, including oxidase–nanozyme cascade reactions that convert analyte-dependent H_2O_2 generation into measurable optical signals. However, nanozymes often exhibit multiple catalytic activities with different relative contributions, making it challenging to tailor their catalytic profiles to specific analytical requirements [14]. Metal composition engineering offers an effective

approach to modulating nanozyme catalysis by altering surface electronic environments and redox characteristics [15–17]. Nevertheless, systematic regulation of catalytic preference through different metal species and composition ratios within a common nanostructural framework remains comparatively underexplored [18, 19].

Beyond metal composition, the interfacial microenvironment plays an important role in regulating substrate interactions and catalytic behavior. Conventional inorganic nanozymes generally lack the chemically diverse environments surrounding natural enzyme active sites, motivating the development of biomimetic surface-functionalization strategies [20, 21]. Protamine (PRTM), a naturally occurring arginine-rich cationic peptide, offers abundant amino and guanidinium groups that can participate in electrostatic interactions and interfacial functionalization. Previous studies have demonstrated the potential of peptide-assisted nanoparticle stabilization and surface engineering [22], while amino-acid-rich interfaces may further influence substrate accessibility and local reaction environments [23, 24]. However, integrating PRTM-mediated interfacial functionalization with metal-composition-dependent catalytic regulation has received limited attention in nanozyme-based colorimetric biosensing. Such an integrated strategy may provide opportunities to tailor catalytic responses while maintaining efficient optical signal transduction.

Here, we developed PRTM-functionalized Au-based multimetallic nanozymes incorporating Pt and Ru (Au@Ru/Pt/PRTM) for colorimetric biosensing (Scheme 1). By comparing their POD- and OXD-like activities and optimizing the Pt/Ru feed ratio, we investigated the influence of metal composition on catalytic preference. The resulting Au@Ru/Pt/PRTM nanozyme exhibited pronounced POD-like activity and was integrated with sarcosine oxidase (SOx) and urate oxidase (UOx) to establish enzyme–nanozyme cascade assays for SA and UA detection, achieving detection limits of 0.75 and 0.0927 μM, respectively. The analytical applicability was further evaluated through selectivity studies and recovery experiments in artificial urine. This work presents a metal-composition-regulated and biomimetically functionalized nanozyme biosensing strategy, highlighting the potential of catalytic preference engineering for sensitive colorimetric biochemical analysis.

Experimental

Materials and instruments

Chloroauric acid trihydrate ($HAuCl_4 \cdot 3H_2O$), uric acid (UA), UOx, glucose (Glu), urea, and L-tryptophan were purchased from Macklin Biochemical Technology Co., Ltd. (Shanghai, China). Chloroplatinic acid hexahydrate ($H_2PtCl_6 \cdot 6H_2O$), Sodium hexachloroiridate(III) hydrate ($Na_3IrCl_6 \cdot xH_2O$), histidine (His), serine (Ser), lysine (Lys), protamine suifate, sodium Carbonate (Na_2CO_3), 2,2'-azino-bis (3-ethylbenzothiazoline-6-sulfonic acid) diammonium salt (ABTS), 3,3',5,5'-tetramethylbenzidine (TMB), and *o*-phenylenediamine (OPD) were obtained from Aladdin (Shanghai, China). Trisodium citrate was purchased from G-clon Beijing Biotechnology Co., Ltd. (Beijing, China). Ruthenium(III) chloride ($RuCl_3$), SA, thiourea (Th), *p*-

benzoquinone(p-BQ), tryptophan (Trp), and palladium(II) chloride dihydrate ($PdCl_2·2H_2O$) were acquired from Adamas-beta (Shanghai, China). Hydrogen peroxide (H_2O_2, 30%) was obtained from Chongqing Chuandong Chemical Co., Ltd. (Chongqing, China). SOx, artificial urine, and sodium acetate buffer (NaAc) were purchased from Shanghai Yuanye Biotech Co., Ltd. (Shanghai, China). Sodium borohydride ($NaBH_4$) was obtained from Chengdu Kelong Chemical Co., Ltd. (Chengdu, China). All reagents were used as received without further purification, and all aqueous solutions were prepared using deionized water.

The morphology and microstructure of the synthesized nanomaterials were characterized by high-resolution transmission electron microscopy (HRTEM; JEOL JEM-2100, Japan), while elemental distributions were examined by energy-dispersive X-ray spectroscopy (EDS; Tecnai G2 F30, FEI, USA). X-ray diffraction (XRD) patterns were collected using a Bruker D8 Advance diffractometer (Germany). X-ray photoelectron spectroscopy (XPS) measurements were performed using a Thermo Scientific K-Alpha spectrometer (USA). Fourier-transform infrared (FT-IR) spectra were recorded using a Thermo Scientific Nicolet iS50 spectrometer (USA). Zeta potentials were measured using a Malvern Zetasizer Nano ZS90 (UK). Electron paramagnetic resonance (EPR) spectra were acquired using a Bruker A300-10/12 spectrometer (Germany). Ultraviolet–visible (UV–vis) absorption spectra were recorded using a TU-1901 spectrophotometer (PERSEE, China), and absorbance at 652 nm was measured using a 1500Pro microplate reader (Shanghai, China).

Preparation of Au NPs.

Gold nanoparticles (Au NPs) were synthesized using a previously reported method with slight modifications [25]. Briefly, an aqueous $HAuCl_4$ solution (88 mL, 1 mM) was brought to a boil in a round-bottom flask equipped with a reflux condenser. Subsequently, 12 mL of trisodium citrate solution (1.0%, w/w) was rapidly added under vigorous stirring, and the reaction mixture was maintained at reflux for 10 min. After cooling naturally to room temperature, the resulting Au NP dispersion was stored at 4°C until further use.

Preparation of Au@Ru/Pt/PRTM.

Au@Ru/Pt/PRTM nanozymes were synthesized according to a previously reported method with minor modifications [26]. The obtained Au NPs (3.2 mL) and PRTM solution (40 μL, 0.1 mg/mL) were sequentially added to ultrapure water (8 mL) and stirred at room temperature for 1 h. Subsequently, H_2PtCl_6 (0.6 mL, 2.5 mM) and $RuCl_3$ (0.6 mL, 2.5 mM) were sequentially introduced, followed by the dropwise addition of freshly prepared, ice-cold $NaBH_4$ solution (0.5 mL, 10 mM). The reaction mixture was stirred at room temperature for an additional 2 h. The resulting product was washed three times with ultrapure water and dried at 60°C for 12 h to obtain Au@Ru/Pt/PRTM nanozymes. Au@Pd/Pt/PRTM and Au@Ir/Pt/PRTM were prepared using the same procedure, with $RuCl_3$ replaced by $PdCl_2$ and Na_3IrCl_6, respectively.

Evaluation of oxidase-like and peroxidase-like activities.

The oxidase (OXD)-like activity of Au@Ru/Pt/PRTM was evaluated using TMB as the chromogenic substrate. Briefly, Au@Ru/Pt/PRTM dispersion (10 μL, 1 mg/mL) and TMB solution (10 μL, 5 mg/mL) were sequentially added to sodium acetate buffer (980 μL, 20 mM, pH 4.5). After incubation at room temperature for 3 min, the absorbance at 652 nm was measured using a microplate reader. The peroxidase (POD)-like activity was evaluated under identical conditions, except that H_2O_2 (10 μL, 0.3%) was introduced into the reaction mixture and the buffer volume was reduced to 970 μL. The absorbance at 652 nm was recorded after incubation at room temperature for 3 min.

Determination of kinetic parameters.

The steady-state kinetic parameters of the nanozymes were determined by monitoring the initial reaction rates at varying substrate concentrations. For OXD-like activity, the TMB concentration was varied from 0.04 to 0.6 mM in the absence of H_2O_2. For POD-like activity, the TMB concentration was varied from 0.01 to 0.1 mM at a fixed H_2O_2 concentration, whereas the H_2O_2 concentration was varied from 0.2 to 6 mM at a fixed TMB concentration. The initial reaction rates were calculated from the time-dependent absorbance changes at 652 nm. Subsequently, the kinetic constants (V_{max} and K_m) were calculated by fitting the Michaelis–Menten equation ($V = V_{max}[S] / (K_m + [S])$), where V is the reaction rate, V_{max} is the maximum reaction rate, [S] is the substrate concentration, and K_m is the Michaelis constant.

Colorimetric detection of SA and UA.

Enzyme–nanozyme cascade colorimetric assays were established for the determination of SA and UA by coupling SOx or UOx with Au@Ru/Pt/PRTM nanozymes, respectively. For SA detection, SA solutions at different concentrations (5 μL, 2.5–100 μM) were incubated with SOx (20 μL, 1 mg/mL) at 37°C for 5 min. Subsequently, Au@Ru/Pt/PRTM (4 μL, 1 mg/mL), NaAc buffer (361 μL, 20 mM, pH 4.5), and TMB solution (10 μL, 5 mg/mL) were sequentially added. After incubation at 37°C for an additional 10 min, the absorbance at 652 nm was recorded. For UA detection, UA solutions at different concentrations (5 μL, 0.25–125 μM) were incubated with UOx (20 μL, 1 mg/mL) at 37°C for 10 min. The subsequent colorimetric reaction was performed under identical conditions to those used for SA detection, and the absorbance at 652 nm was measured after incubation at 37°C for 10 min.

Detection of SA and UA in real samples.

The analytical applicability of the proposed colorimetric assays was evaluated using artificial urine as a model biological matrix. Sample pretreatment was performed according to a previously reported procedure with minor modifications [27]. Briefly, artificial urine samples were diluted 20-fold before analysis, and the background concentrations of SA and UA were determined using the unspiked samples. To assess analytical accuracy and matrix effects, known amounts of SA or UA were spiked into the diluted artificial urine at three concentration levels (low, medium, and high). According to the method

described in the colorimetric detection section, the accuracy of Au@Ru/Pt/PRTM nanozymes for the determination of SA and UA was evaluated.

Results and discussion

Synthesis and characterization of Au@Ru/Pt/PRTM nanozymes

Au@Ru/Pt/PRTM nanozymes were fabricated through a stepwise synthesis and surface-functionalization strategy (Fig. 1A). Citrate-stabilized Au nanoparticles (Au NPs) were first prepared as seeds, followed by the incorporation of Pt and Ru species in the presence of PRTM. TEM images exhibited nearly spherical morphologies with relatively uniform particle sizes and good dispersibility for both Au NPs and Au@Ru/Pt/PRTM (Fig. 1B,C). The average particle diameter increased from 11.27 to 14.87 nm following modification (Fig. S1), consistent with the incorporation of additional components. HRTEM image revealed distinct lattice fringes, indicating crystalline metallic domains (Fig. 1D). HAADF-STEM image and corresponding elemental maps demonstrated the spatial colocalization of Au, Pt, Ru, C, N, and O (Fig. 1E), supporting the incorporation of the multimetallic components and the presence of an organic interface. Zeta-potential measurements further revealed a change in surface properties during synthesis (Fig. 1F). Citrate-stabilized Au NPs exhibited a negative potential of − 19.0 mV, whereas free PRTM displayed a positive potential of + 5.6 mV, suggesting that electrostatic interactions could facilitate their association. Following Pt/Ru incorporation and PRTM functionalization, the zeta potential shifted to − 16.7 mV, indicating modification of the surface charge environment.

The FT-IR spectroscopy was employed to investigate the surface functional groups and interfacial chemical environment of Au@Ru/Pt/PRTM (Fig. S2). Citrate-stabilized Au NPs exhibited a broad absorption band at approximately 3439 cm^{-1}, attributed to O–H stretching vibrations, together with two characteristic bands at 1604 and 1391 cm^{-1} assigned to the asymmetric and symmetric stretching vibrations of citrate-derived carboxylate groups, respectively [28]. Following Pt/Ru incorporation and PRTM functionalization, these bands exhibited noticeable shifts and broadening, suggesting changes in the surface coordination environment and possible interactions between the organic and metallic components [29]. The accompanying changes in optical properties were examined by UV–vis absorption spectroscopy (Fig. 2A). Pristine Au NPs displayed a characteristic localized surface plasmon resonance (LSPR) band centered at approximately 520 nm [30]. After modification, the absorption profile broadened and shifted slightly toward longer wavelengths, with increased absorption extending into the visible and near-infrared regions. These spectral changes may be associated with variations in particle size, metal composition, and the local dielectric environment [31]. X-ray diffraction (XRD) analysis was further performed to evaluate the crystalline structure (Fig. 2B). Au NPs exhibited diffraction peaks at approximately 38.2°, 44.4°, 64.6°, 77.5°, and 81.7°, corresponding to the (111), (200), (220), (311), and (222) planes of face-centered cubic (fcc) Au (PDF No. 04-0784), respectively [32]. These characteristic reflections were largely preserved in Au@Ru/Pt/PRTM, indicating that the crystalline Au framework

remained intact following modification. The absence of distinct Pt- and Ru-related reflections may result from overlapping diffraction peaks, small crystallite dimensions, or relatively low contents of the incorporated metals [33].

To further elucidate the surface elemental composition and chemical states of Au@Ru/Pt/PRTM, XPS was performed. The survey spectrum confirmed the presence of Au, Pt, Ru, C, N, and O (Fig. 2C). The high-resolution Au 4f spectrum exhibited characteristic peaks at 84.25 and 87.90 eV, corresponding to Au $4f_{7/2}$ and Au $4f_{5/2}$, respectively, consistent with metallic Au (Fig. 2D). The Pt 4f spectrum was deconvoluted into two spin–orbit doublets assigned to Pt^0 and Pt^{2+} species (Fig. 2E), with the dominant Pt^0 peaks located at 71.79 and 74.95 eV. Similarly, the Ru 3p spectrum indicated the coexistence of Ru^0 and Ru^{4+} species (Fig. 2F) [34]. Given the spectral overlap between Ru 3d and C 1s, the corresponding region was fitted by considering contributions from both ruthenium and carbon-containing species [35–37]. The fitted Ru 3d components further supported the presence of metallic and oxidized Ru species (Fig. 2G), consistent with the Ru 3p analysis. Meanwhile, the C 1s spectrum displayed components at 284.59, 286.17, and 288.02 eV, assigned to C–C/C–H, C–O/C–N, and C = O/carboxylate species, respectively (Fig. 2G). The N 1s spectrum exhibited components associated with N–H, C–N, and C = N environments (Fig. 2H), consistent with the amino- and guanidinium-rich structure of PRTM, while the O 1s spectrum revealed contributions from C = O and C–O species (Fig. 2I). These organic functionalities were consistent with the presence of residual citrate and a PRTM-associated interfacial layer. Together with the preceding FT-IR, UV–vis, and XRD analyses, these findings supported the incorporation of Pt and Ru into the Au-based nanostructure and the formation of an organic–metallic interface while preserving the crystalline Au framework. The coexistence of multiple metal oxidation states and surface organic functionalities may influence substrate adsorption and interfacial redox processes, thereby establishing a structural foundation for subsequent investigations into the catalytic activity of Au@Ru/Pt/PRTM.

Regulation of POD- and OXD-like catalytic activities of Au@Ru/Pt/PRTM nanozymes

The proposed OXD- and POD-like catalytic pathways of Au@Ru/Pt/PRTM were illustrated in Fig. 3A. Under OXD-like conditions, the nanozyme may facilitate molecular oxygen activation and superoxide radical ($\bullet O_2^-$) generation, promoting the oxidation of TMB to its oxidized form (oxTMB). In contrast, POD-like catalysis involves H_2O_2 activation and the generation of reactive oxygen species, including hydroxyl radicals (•OH), which facilitate TMB oxidation. To evaluate the substrate dependence of POD-like activity, three chromogenic substrates, TMB, ABTS, and OPD, were examined in the presence of H_2O_2. As shown in Fig. 3B, TMB produced the strongest colorimetric response, with a characteristic absorption peak at 652 nm, whereas OPD exhibited a weaker response and ABTS showed negligible oxidation. These results revealed pronounced substrate-dependent catalytic behavior and support the selection of TMB for subsequent colorimetric assays.

To investigate the influence of material composition on catalytic performance, the POD-like activities of Au NPs, Pt@PRTM, and Au@Au/Pt/PRTM were first compared (Fig. 3C). Pristine Au NPs exhibited negligible catalytic activity, whereas Pt@PRTM generated a pronounced oxTMB signal. Au@Au/Pt/PRTM displayed the strongest response, suggesting that integration of the Au framework with Pt-containing components and PRTM functionalization improved the overall catalytic performance. Subsequently, different metals (Pd, Ir, and Ru) were incorporated to further modulate the catalytic properties. All trimetallic nanozymes exhibited enhanced POD-like activity compared with Au@Au/Pt/PRTM, with Au@Ru/Pt/PRTM showing the highest activity, followed by Au@Ir/Pt/PRTM and Au@Pd/Pt/PRTM (Fig. 3D). Interestingly, the OXD-like activities exhibited a different trend, with Au@Pd/Pt/PRTM displaying the strongest response, followed by Au@Ir/Pt/PRTM and Au@Au/Pt/PRTM, whereas Au@Ru/Pt/PRTM showed the weakest activity (Fig. 3E). These contrasting activity profiles indicated that metal incorporation not only affects catalytic performance but also influences the relative preference for POD- and OXD-like reactions, highlighting the potential of metal-composition engineering for tailoring nanozyme catalytic behavior.

The effect of metal composition was further investigated by varying the Pt/Ru feed ratio. The POD-like activity reached its maximum at a Pt/Ru ratio of 2:8 (Fig. 3F), whereas the highest OXD-like activity was observed at a ratio of 6:4 (Fig. S3), further supporting the composition-dependent regulation of catalytic preference. The reaction conditions were subsequently optimized to maximize the POD-like response for colorimetric sensing. Au@Ru/Pt/PRTM exhibited appreciable POD-like activity over a pH range of 4.5–6.0, with an optimum at pH 4.5, while its OXD-like activity remained comparatively low under the tested conditions (Fig. 3G). Increasing the nanozyme concentration enhanced the reaction rate and oxTMB formation (Fig. 3H). Although 15 μg/mL produced a slightly faster initial response, the reaction profiles at 10 and 15 μg/mL approached similar plateaus. Accordingly, 10 μg/mL was selected to balance catalytic performance and material consumption. The optimal reaction temperature was determined to be 35°C (Fig. S4). The storage stability of Au@Ru/Pt/PRTM was also evaluated (Fig. S5). After storage at room temperature or 4°C for 30 days, the nanozyme retained most of its initial catalytic activity, indicating satisfactory stability under the investigated conditions. These results demonstrated that metal composition provided an effective means of modulating the relative POD- and OXD-like activities of Au-based nanozymes. Particularly, Au@Ru/Pt/PRTM combines pronounced POD-like activity with favorable operational conditions and storage stability, supporting its application as a catalytic signal-amplification component in colorimetric biosensing.

Kinetic Determination of Au@Ru/Pt/PRTM and Free-Radical Analysis

To quantitatively evaluate the influence of metal composition on nanozyme catalysis, steady-state kinetic analyses were performed by varying the concentrations of TMB or H_2O_2 under POD- and OXD-like reaction conditions. The initial reaction velocities increased with substrate concentration and gradually approached saturation, exhibiting typical Michaelis–Menten behavior (Fig. 4A–I). The experimental data were fitted to the Michaelis–Menten model to determine the apparent maximum reaction velocity (V_{max})

and Michaelis constant (K_m). The corresponding Lineweaver–Burk plots showed approximately linear relationships (Fig. S6–S8), consistent with the observed saturation kinetics.

For POD-like catalysis, the kinetic parameters obtained by varying the TMB concentration revealed distinct metal-dependent differences (Fig. 4A–C). The V_{max} values of Au@Pd/Pt/PRTM, Au@Ir/Pt/PRTM, and Au@Ru/Pt/PRTM were 5.3418, 11.4773, and 14.9970 × 10^{-8} M s^{-1}, respectively, with corresponding K_m values of 0.0254, 0.0553, and 0.0443 mM. Notably, Au@Ru/Pt/PRTM exhibited a V_{max} approximately 2.8-fold higher than that of Au@Pd/Pt/PRTM, indicating enhanced catalytic conversion of TMB under POD-like conditions. Although Au@Pd/Pt/PRTM displayed the lowest apparent K_m, its V_{max} was substantially lower, suggesting that a smaller K_m does not necessarily correspond to a higher catalytic rate. Importantly, K_m reflects both substrate association and catalytic turnover and should not be interpreted solely as a measure of substrate-binding affinity [38]. When H_2O_2 was used as the variable substrate, a similar trend was observed (Fig. 4D–F). The V_{max} values increased from 13.6175 × 10^{-8} M s^{-1} for Au@Pd/Pt/PRTM to 17.2549 × 10^{-8} M s^{-1} for Au@Ir/Pt/PRTM and 24.4076 × 10^{-8} M s^{-1} for Au@Ru/Pt/PRTM, whereas the corresponding K_m values decreased from 2.4721 to 1.2172 and 1.0887 mM, respectively. These results demonstrated that Au@Ru/Pt/PRTM exhibited the highest apparent catalytic capacity toward both POD substrates among the investigated nanozymes.

In contrast, the OXD-like kinetic profiles exhibited a different metal-dependent trend (Fig. 4G–I and Table S1). Au@Pd/Pt/PRTM showed the highest V□□□ (4.8060 × 10^{-8} M s^{-1}), followed by Au@Ir/Pt/PRTM (3.8840 × 10^{-8} M s^{-1}) and Au@Ru/Pt/PRTM (3.3464 × 10^{-8} M s^{-1}). The corresponding K_m values for TMB were 0.0691, 0.0666, and 0.0157 mM, respectively. Interestingly, Au@Ru/Pt/PRTM exhibited the lowest apparent K_m but the lowest V_{max} under OXD-like conditions, further indicating that substrate-dependent saturation behavior and maximum catalytic capacity are not necessarily correlated. More importantly, the contrasting V_{max} trends observed for POD- and OXD-like reactions demonstrated that metal composition influences the relative catalytic preference of the nanozymes. In particular, Ru incorporation favors a higher POD-like response, whereas Pd-containing nanozymes exhibit comparatively stronger OXD-like activity under the investigated conditions.

To investigate the reactive oxygen species (ROS) involved in POD-like catalysis, radical scavenging experiments were performed using p-BQ, Th, and Trp as scavengers for superoxide radicals ($\bullet O_2^-$), hydroxyl radicals (•OH), and singlet oxygen ($^1O_2$), respectively [39]. The addition of these scavengers suppressed TMB oxidation in a concentration-dependent manner (Fig. S9), suggesting the possible involvement of multiple ROS. EPR spectroscopy was subsequently employed to further examine ROS generation. As shown in Fig. 4J, no discernible •OH-related signal was observed in the control group, whereas characteristic radical-adduct signals appeared in the Au@Ru/Pt/PRTM catalytic system and increased from 5 to 10 min, supporting time-dependent •OH generation during H_2O_2 activation. Additional EPR signals assigned to $\bullet O_2^-$ and $^1O_2$ were observed (Fig. S10). The scavenging experiments and EPR results both confirmed that various ROS are involved in this catalytic reaction.

Finally, the apparent kinetic parameters of Au@Ru/Pt/PRTM were compared with those of representative natural enzymes and previously reported nanozymes (Fig. 4K and Table S2). Au@Ru/Pt/PRTM exhibited relatively low K_m values toward both TMB and H_2O_2 compared with most catalysts included in the comparison. Together with its high V_{max}, particularly for H_2O_2-dependent catalysis, these results highlight its favorable kinetic performance under the investigated conditions. Overall, the composition-dependent kinetic behavior and ROS-generation characteristics support the selection of Au@Ru/Pt/PRTM as the catalytic component for subsequent enzyme–nanozyme cascade colorimetric detection of UA and SA.

Colorimetric detection of UA and SA using Au@Ru/Pt/PRTM nanozymes

Building on the favorable POD-like activity of Au@Ru/Pt/PRTM, an oxidase–nanozyme cascade colorimetric platform was developed for the determination of UA and SA (Fig. 5A). The cascade systems couple enzymatic H_2O_2 generation with nanozyme-mediated chromogenic reactions, providing a convenient approach for signal transduction in biomarker analysis [40, 41]. SA has been investigated as a potential prostate cancer-associated biomarker, whereas UA is clinically relevant to hyperuricemia, gout, and renal dysfunction [42, 43].In the proposed assays, SA and UA were oxidized by SOx and UOx, respectively, producing H_2O_2. The generated H_2O_2 was subsequently utilized by Au@Ru/Pt/PRTM to catalyze the oxidation of TMB into blue-colored oxTMB, enabling quantitative determination of the analytes through absorbance measurements at 652 nm.

The analytical performance of the SOx/Au@Ru/Pt/PRTM cascade system was first evaluated for SA detection. The absorbance at 652 nm increased progressively with SA concentration over the range of 2.5–100 μM (Fig. 5B), exhibiting a linear relationship described by $\Delta A = 0.0122 + 0.0048C_{SA}$ ($R^2 = 0.9937$) (Fig. 5C). The limit of detection (LOD), calculated using the 3σ/k criterion, was 0.75 μM. Compared with previously reported SA sensing methods, the proposed assay exhibited comparable analytical performance while offering a straightforward colorimetric readout (Table S3). The selectivity was further assessed against common urinary constituents, including UA, urea, glucose, amino acids (lysine, histidine, and serine), and inorganic ions (Na^+, K^+, Mg^{2+}, Ca^{2+}, Fe^{3+}, Cl^-, SO_4^{2-}, HPO_4^{2-}, and CO_3^{2-}). As shown in Fig. 5D, SA produced a substantially stronger response than the tested interferents. Moreover, the presence of these substances caused only minor variations in the SA signal (Fig. S11), indicating satisfactory selectivity and resistance to interference under the investigated conditions.

The platform was subsequently extended to UA detection using the UOx/Au@Ru/Pt/PRTM cascade system. A concentration-dependent increase in absorbance was observed (Fig. 5E), yielding a linear calibration equation of $\Delta A = 0.0176 + 0.0033C_{UA}$ ($R^2 = 0.9983$) (Fig. 5F). The calculated LOD was 0.0927 μM, demonstrating high analytical sensitivity. Comparison with previously reported colorimetric UA assays further indicated competitive detection performance (Table S4). Selectivity experiments revealed a markedly stronger response toward UA than toward the tested interfering species (Fig. 5G), while the

UA signal remained relatively stable in the presence of coexisting substances (Fig. S12). These findings demonstrated that the proposed cascade strategy enables sensitive and selective colorimetric determination of SA and UA through analyte-specific enzymatic recognition.

To evaluate the applicability of the developed assays in a biological matrix, the recovery experiments were performed using artificial urine samples (Table S5). SA was not detected in the unspiked artificial urine, whereas an apparent UA concentration of 8.28 μM was measured. The recoveries ranged from 91.25% to 96.49% for SA and from 89.20% to 92.53% for UA, with corresponding relative standard deviations (RSDs) of 1.18%–1.56% and 1.54%–2.44%, respectively. These results indicated acceptable analytical recovery and repeatability in the tested artificial urine matrix. Overall, the oxidase–Au@Ru/Pt/PRTM cascade platform provided a sensitive and convenient approach for the colorimetric determination of SA and UA, highlighting its potential for biochemical sensing applications.

Conclusion

In summary, we developed a metal-composition-regulated and protamine-functionalized nanozyme platform for sensitive colorimetric biosensing. By incorporating different metal species into Au-based nanozymes, we demonstrated composition-dependent modulation of POD- and OXD-like catalytic activities, highlighting the role of metal composition in tailoring catalytic preference. The optimized Au@Ru/Pt/PRTM nanozyme exhibited favorable POD-like catalytic performance and was integrated with natural oxidases to establish cascade biosensing assays for SA and UA, achieving detection limits of 0.75 and 0.0927 μM, respectively. The assays also demonstrated satisfactory selectivity, resistance to interference, and analytical recoveries in spiked artificial urine samples. These findings highlight the potential of integrating metal-composition engineering with biomimetic interfacial functionalization to develop versatile nanozyme-based biosensors, offering a promising strategy for sensitive and reliable biochemical analysis.

Declarations

Acknowledgements

Not applicable.

Author Contributions Statement

All authors contributed to the article and approved the final manuscript. Qiu Mao & Lin He: Methodology, Investigation, Writing – original draft. Huajia Xu & Mingmeng Xie& Siqiao Li: Validation, Software, Investigation, Formal analysis, Funding acquisition. Shudong Cao& Dan He & Zhengwei Zhang: Writing – review & editing, Visualization, Supervision, Funding acquisition.

Funding

This work was funded by the National Natural Science Foundation of China (82372350), Natural Science Foundation Project of Chongqing (CSTB2025NSCQ-GPX1170), Youth Project of Science and Technology Research Program of Chongqing Education Commission of China (KJQN202400478).

Data availability

No datasets were generated or analysed during the current study.

Ethics approval and consent to participate

Not applicable.

Consent for publication

Not applicable.

Competing interests

The authors declare no competing interests.

Declaration of AI-assisted writing

ChatGPT was used solely for English language polishing and grammatical refinement of the manuscript. No AI tools were used to generate, modify, or enhance any figures or graphical abstracts.

References

1. Levin A, Ahmed SB, Carrero JJ et al (2024) Executive summary of the KDIGO 2024 Clinical Practice Guideline for the Evaluation and Management of Chronic Kidney Disease: known knowns and known unknowns. Kidney Int 105:684–701. http://doi.org/10.1016/j.kint.2023.10.016
2. Cheng JG, Wu YF, Zhu LJ et al (2024) Uric acid biosensors based on molecular recognition: Classifications, advances, and prospects. Trac-Trend Anal Chem 179:117887. http://doi.org/10.1016/j.trac.2024.117887
3. Onifade OA, Yusairie FA, Bakar MH et al (2024) Uricase biofunctionalized plasmonic sensor for uric acid detection with APTES-modified gold nanotopping. Biosens Bioelectron 261:116486. http://doi.org/10.1016/j.bios.2024.116486
4. Pujana-Vaquerizo M, Bozal-Basterra L, Carracedo A (2024) Metabolic adaptations in prostate cancer. Br J Cancer 131:1250–1262. http://doi.org/10.1038/s41416-024-02762-z
5. Yang X, Lu Z, Wu W et al (2025) Multilayered sandwich structure sensor: Confinement-mediated H_2O_2 enrichment strategy for ultrasensitive and long-term stable prostate cancer biomarker detection. Small 21:e05472. http://doi.org/10.1002/smll.202505472
6. Liu P, Sun Q, Gai ZX, Yang F, Yang YZ (2026) Dual-mode fluorescence and colorimetric smartphone-based sensing platform with oxidation-induced self-assembled nanoflowers for sarcosine detection.

Anal Chim Acta 1306:342586. http://doi.org/10.1016/j.aca.2024.342586

7. Jia WJ, Zhu B, Xiang DQ et al (2025) Peroxidase nanozyme-incorporated sponge: A smartphone-enabled dual-mode visual sensing platform for trace uric acid detection via a shape-memory effect-driven signal amplification strategy. Biosens Bioelectron 283:117541. http://doi.org/10.1016/j.bios.2025.117541
8. Pardhi N, Cheng W-C, Chen S-C, Sun H, Govindasamy M (2025) Amperometric sensing of prostate cancer biomarker (Sarcosine) using HiPIMS deposited nickel nitride films-decorated zinc oxide nanorod heterostructures. Appl Surf Sci Adv 27:100741. http://doi.org/10.1016/j.apsadv.2025.100741
9. Zhang Z, Hu JJ, Lin S et al (2024) Field effect transistor biosensors for healthcare monitoring. Interdiscip Med 2:e20240032. http://doi.org/10.1002/inmd.20240032
10. Li M, Wang L, Xu A et al (2024) Rapid and Sensitive Biosensing of Salmonella Using Mechanical Step Rotation and Gold@platinum Nanozymatic Amplification. J Anal Test 8:262–269. http://doi.org/10.1007/s41664-024-00313-2
11. Wang L, Li M, Xu A, Li Y, Lin J (2025) Lab-on-a-Syringe Biosensing of Salmonella using Magnetic Grid Separation with Nanozyme Signal Amplification. J Anal Test 9:12–20. http://doi.org/10.1007/s41664-024-00339-6
12. Li J, Duan L, Chen Q et al (2025) Roles of nanomagnetic beads on biosensing: From fabrication to application. Interdiscip Med 3:e20250030. http://doi.org/10.1002/inmd.20250030
13. Chen Z, Yu Y, Gao Y, Zhu Z (2023) Rational Design Strategies for Nanozymes. ACS Nano 17:13062–13080. http://doi.org/10.1021/acsnano.3c04378
14. Fan H, Zhang R, Fan K, Gao L, Yan X (2024) Exploring the specificity of nanozymes. ACS Nano 18:2533–2540. http://doi.org/10.1021/acsnano.3c07680
15. Liu SY, Liu ZQ, Chen L et al (2025) Pt nanoparticles modified single-atoms nanozymes with tunable metal valence for rapid chlorpyrifos colorimetric detection. Biosens Bioelectron 287:117730. http://doi.org/10.1016/j.bios.2025.117730
16. Saha D, Tang C, Khan J et al (2026) Alkaline electrocatalytic water oxidation by Fe–Ni nanostructures on porous turbostratic carbon with tailorable metal–metal active sites. Chem Sci 17:3841–3856. http://doi.org/10.1039/d5sc05330g
17. Singh K, Maurya KK, Malviya M (2024) Review of electrochemical sensors and biosensors based on first-row transition metals, their oxides, and noble metals nanoparticles. J Anal Test 8:143–159. http://doi.org/10.1007/s41664-023-00292-w
18. Xu GP, Liu KH, Jia BQ et al (2024) Electron Lock Manipulates the Catalytic Selectivity of Nanozyme. ACS Nano 18:3814–3825. http://doi.org/10.1021/acsnano.3c12201
19. Zare I, Choi D, Zhang JY et al (2024) Modulating the catalytic activities of nanozymes for molecular sensing. Nano Today 56:102276. http://doi.org/10.1016/j.nantod.2024.102276
20. Li T, Wang XY, Wang YT et al (2024) Microenvironmental modulation breaks intrinsic pH limitations of nanozymes to boost their activities. Nat Commun 15:10861. http://doi.org/10.1038/s41467-024-

55163-4

21. Liang H, Chen X, Bu Z et al (2024) When nanozymes meet deoxyribonucleic acid: Understanding their interactions and biomedical diagnosis applications. Interdiscip Med 2:e20230057. http://doi.org/10.1002/inmd.20230057
22. Huo XB, Wang XF, Ding KX et al (2026) Protamine-modified CuAu nanocarrier enhances aptamer-mediated synergistic therapy for breast cancer. Int J Biol Macromol 371:153013. http://doi.org/10.1016/j.ijbiomac.2026.153013
23. Wu J, Liang L, Li SS et al (2024) Rational design of nanozyme with integrated sample pretreatment for colorimetric biosensing. Biosens Bioelectron 257:116310. http://doi.org/10.1016/j.bios.2024.116310
24. Ashrafi AM, Mukherjee A, Saadati A et al (2024) Enhancing the substrate selectivity of enzyme mimetics in biosensing and bioassay: Novel approaches. Adv Colloid Interface Sci 331:103233. http://doi.org/10.1016/j.cis.2024.103233
25. Zhang Q, He L, Rani KK et al (2021) Colorimetric detection of neomycin sulfate in tilapia based on plasmonic core-shell Au@PVP nanoparticles. Food Chem 356:129612. http://doi.org/10.1016/j.foodchem.2021.129612
26. Liu Y, Qin Y, Zhang Q et al (2021) Arginine-rich peptide/platinum hybrid colloid nanoparticle cluster: A single nanozyme mimicking multi-enzymatic cascade systems in peroxisome. J Colloid Interface Sci 600:37–48. http://doi.org/10.1016/j.jcis.2021.05.025
27. Ma ZQ, Yang LJ, Wang YT et al (2021) Construction and stabilization of a peptide-based peroxidase mimic for the colorimetric detection of uric acid and sarcosine. Chem Eng J 416:129149. http://doi.org/10.1016/j.cej.2021.129149
28. Wulandari P, Nagahiro T, Fukada N et al (2015) Characterization of citrates on gold and silver nanoparticles. J Colloid Interface Sci 438:244–248. http://doi.org/10.1016/j.jcis.2014.09.078
29. Park JW, Shumaker-Parry JS (2014) Structural study of citrate layers on gold nanoparticles: role of intermolecular interactions in stabilizing nanoparticles. J Am Chem Soc 136:1907–1921. http://doi.org/10.1021/ja4097384
30. Vinnacombe-Willson GA, Conti Y, Stefancu A et al (2023) Direct bottom-up in situ growth: A paradigm shift for studies in wet-chemical synthesis of gold nanoparticles. Chem Rev 123:8488–8529. http://doi.org/10.1021/acs.chemrev.2c00914
31. Han HH, Kim SJ, Kim J et al (2023) Bimetallic hyaluronate-modified Au@Pt nanoparticles for noninvasive photoacoustic imaging and photothermal therapy of skin cancer. ACS Appl Mater Interfaces 15:11609–11620. http://doi.org/10.1021/acsami.3c01858
32. Liu SJ, Shu R, Jia HL et al (2025) Antibody-level bacteria grabbing by mechanic invasion of bioinspired hedgehog artificial mesoporous nanostructure for hierarchical dynamic Identification and light-response sterilization. Adv Mater 37:2416906. http://doi.org/10.1002/adma.202416906
33. Bezerra LS, Brasseur P, Sullivan-Allsop S et al (2024) Ultralow catalytic loading for optimised electrocatalytic performance of AuPt nanoparticles to produce hydrogen and ammonia. Angew

Chem Int Ed Engl 63:e202405459. http://doi.org/10.1002/anie.202405459

34. Qiao CF, Sun ZY, Muhammad F et al (2025) Ruthenium oxide nanozyme for tendinopathy treatment via countering ferroptosis. Adv Healthc Mater 14:2501035. http://doi.org/10.1002/adhm.202501035
35. Zhong S, Zhang Z, Zhao Q et al (2024) Lattice expansion in ruthenium nanozymes improves catalytic activity and electro-responsiveness for boosting cancer therapy. Nat Commun 15:8097. http://doi.org/10.1038/s41467-024-52277-7
36. Duan Z, Li P, Wang Y et al (2026) Biomimetic Ru-Mn nanozyme with cascade catalytic activity attenuates secondary brain injury in intracerebral hemorrhage. Adv Sci 13:e19340. http://doi.org/10.1002/advs.202519340
37. Wang D, Zhao S, Li J, Shi L, Zhang Y (2024) Defect-rich RuO_2/IrO_2 heterojunction with dual enzyme-mimic activities for boosting biocatalytic disinfection. Chem Eng J 481:148888. http://doi.org/10.1016/j.cej.2024.148888
38. Liu C, Zhang M, Geng HQ et al (2021) NIR enhanced peroxidase-like activity of Au@CeO2 hybrid nanozyme by plasmon-induced hot electrons and photothermal effect for bacteria killing. Appl Catal B-Environ 295:120317. http://doi.org/10.1016/j.apcatb.2021.120317
39. Luo JJ, Zhao SC, Wu D et al (2025) Urea-assisted fabrication of defect and oxygen vacancy-enriched Ce $(MoO_4)_2$ oxidase mimetics: A dual-mode sensor array for detection and recognition of phenolic antioxidants. Sens Actuat B-Chem 424:136922. http://doi.org/10.1016/j.snb.2024.136922
40. Hu XY, Zhu TB, Zhang GX, Ye ZC, Chen XL (2024) Ru nanosheets with specific peroxidase activity for biosensor applications. Sens Actuat B-Chem 394:134478. http://doi.org/10.1016/j.snb.2023.134478
41. Hou BB, Guo XY, Zhang Y et al (2023) Rational atomic engineering of prussian blue analogues as peroxidase mimetics for colorimetric urinalysis of uric acid. ACS Sustain Chem Eng 11:6211–6219. http://doi.org/10.1021/acssuschemeng.2c07286
42. Johnson RJ, Mandell BF, Schlesinger N et al (2024) Controversies and practical management of patients with gout and chronic kidney disease. Kidney Int 106:573–582. http://doi.org/10.1016/j.kint.2024.05.033
43. Liu WT, Wang XJ, Dong BJ, Liu YQ, Wei DC (2024) Enzymatic cascade reactors on carbon nanotube transistor detecting trace prostate cancer biomarker. Biosens Bioelectron 263:116603. http://doi.org/10.1016/j.bios.2024.116603

Schemes

Scheme 1 is available in the Supplementary Files section

Figures

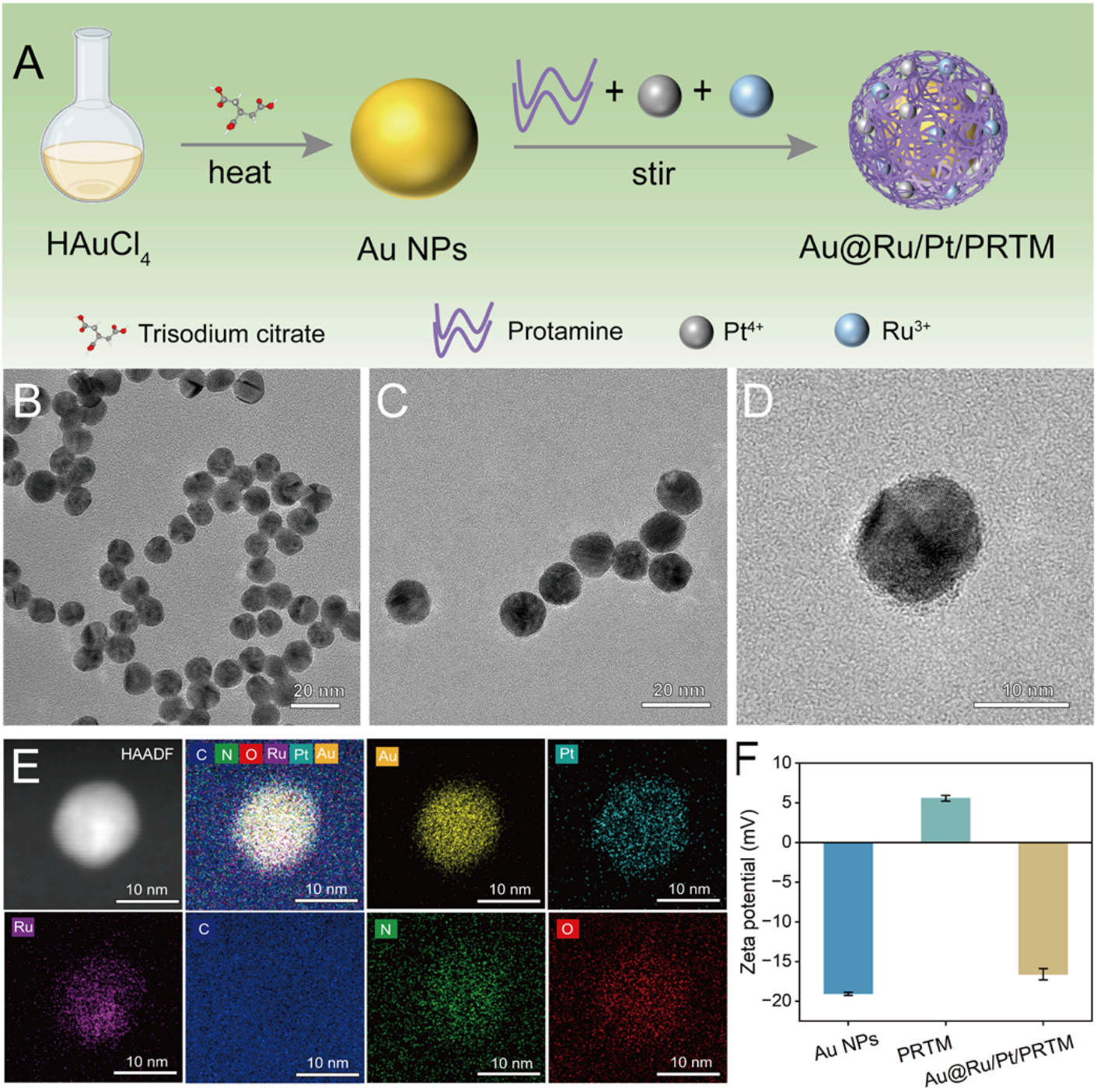

Figure 1

(A) Schematic illustration of the stepwise synthesis of Au@Ru/Pt/PRTM. (B,C) TEM images of Au NPs and Au@Ru/Pt/PRTM. (D) HRTEM image of Au@Ru/Pt/PRTM. (E) HAADF-STEM image and corresponding elemental maps of Au, Pt, Ru, C, N, and O for Au@Ru/Pt/PRTM. (F) Zeta potentials of Au NPs, PRTM, and Au@Ru/Pt/PRTM.

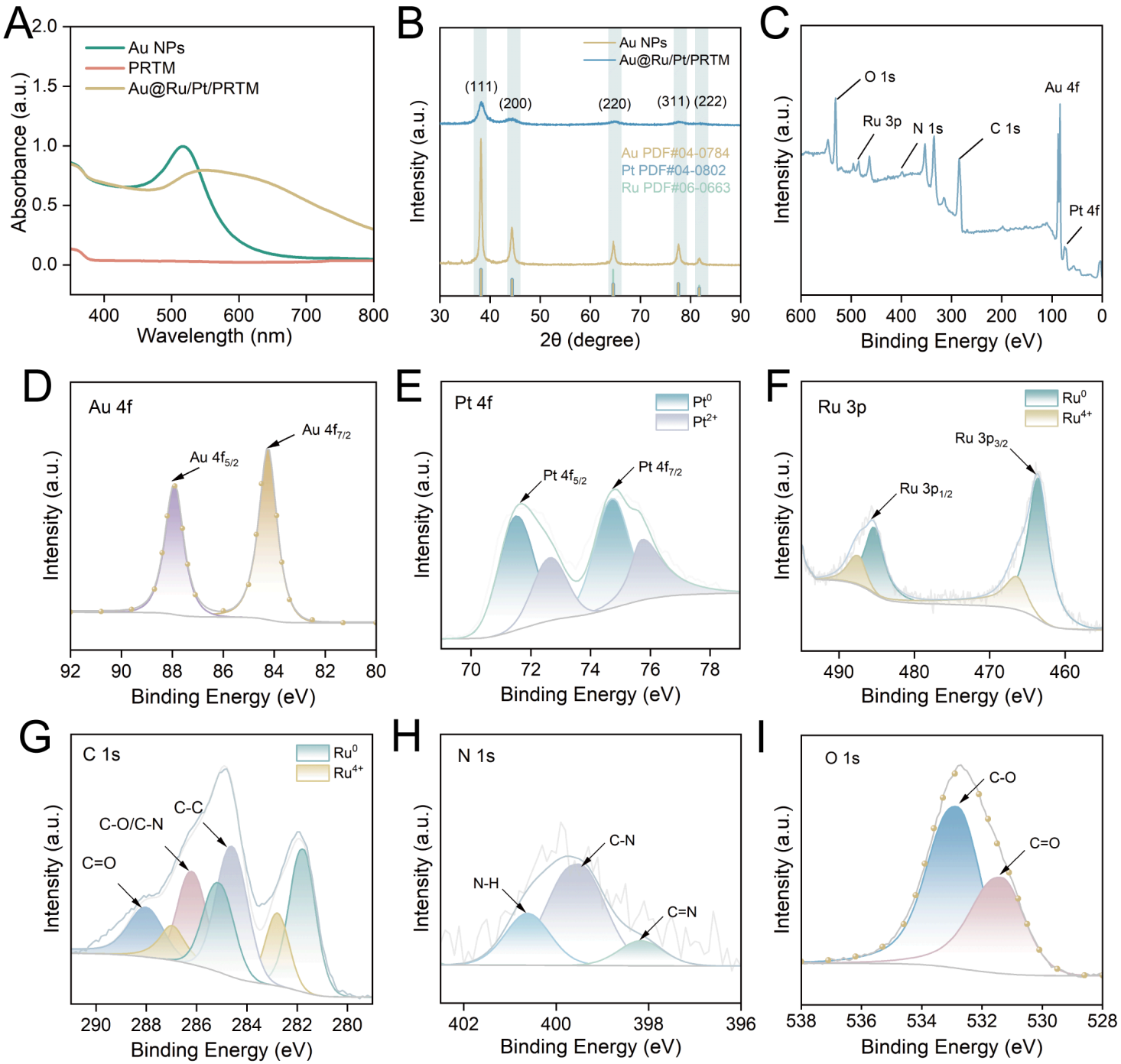

Figure 2

(A) UV–vis absorption spectra of Au NPs, PRTM, and Au@Ru/Pt/PRTM. (B) XRD patterns of Au NPs and Au@Ru/Pt/PRTM. (C) XPS survey spectrum of Au@Ru/Pt/PRTM. High-resolution XPS spectra of (D) Au 4f, (E) Pt 4f, (F) Ru 3p, (G) C 1s, (H) N 1s, and (I) O 1s.

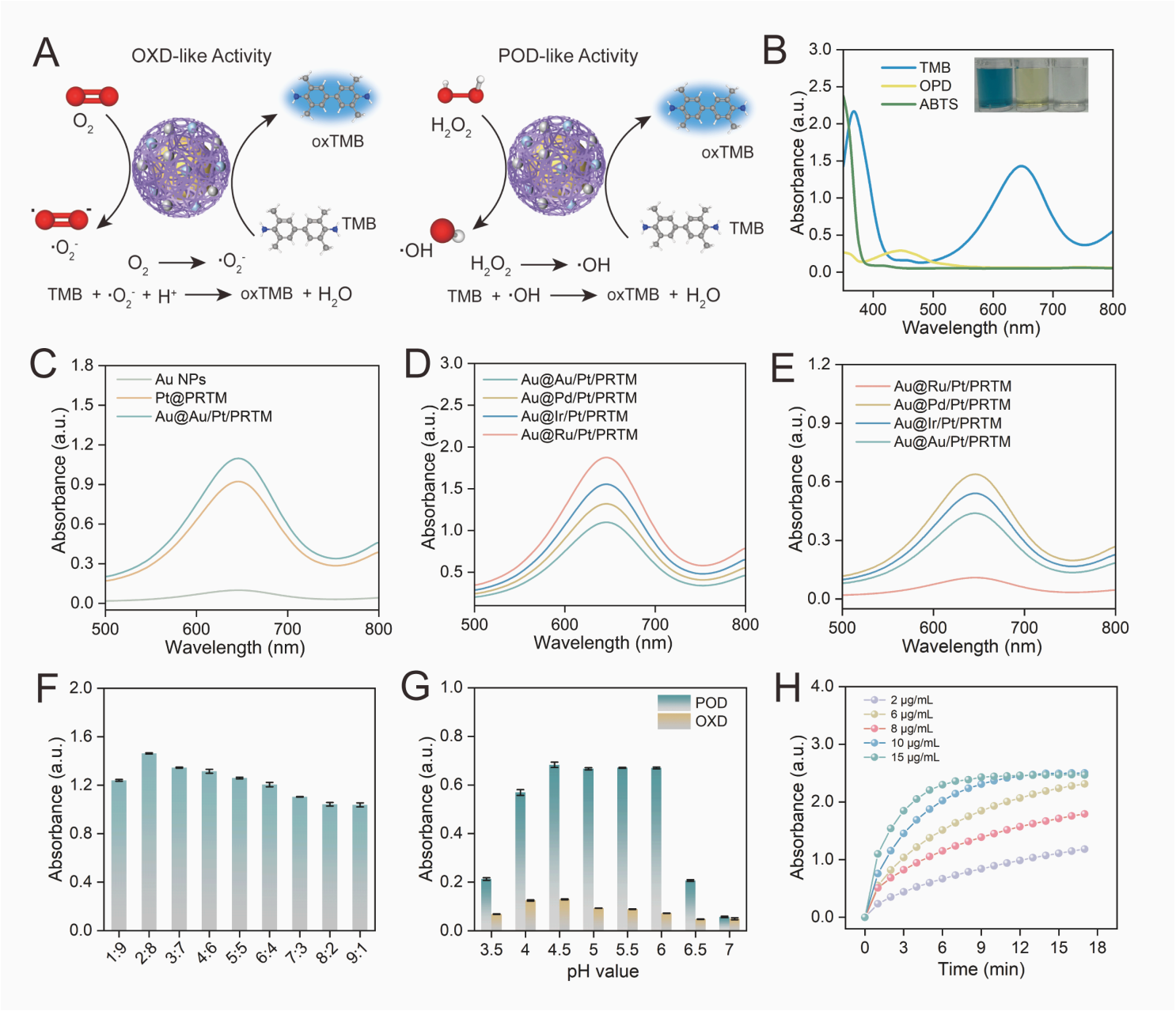

Figure 3

(A) Schematic illustration of the OXD and POD-like catalytic mechanisms. (B) Chromogenic substrate screening using TMB, ABTS, and OPD. (C) POD-like activities of Au NPs, Pt@PRTM, and Au@Au/Pt/PRTM. (D, E) POD- and OXD-like activities of Au@M/Pt/PRTM nanozymes (M = Au, Pd, Ir, or Ru). (F) Effect of the Pt/Ru ratio on POD-like activity. (G) pH-dependent POD- and OXD-like activities of Au@Ru/Pt/PRTM. (H) Time-dependent POD-like catalytic responses of Au@Ru/Pt/PRTM at different concentrations.

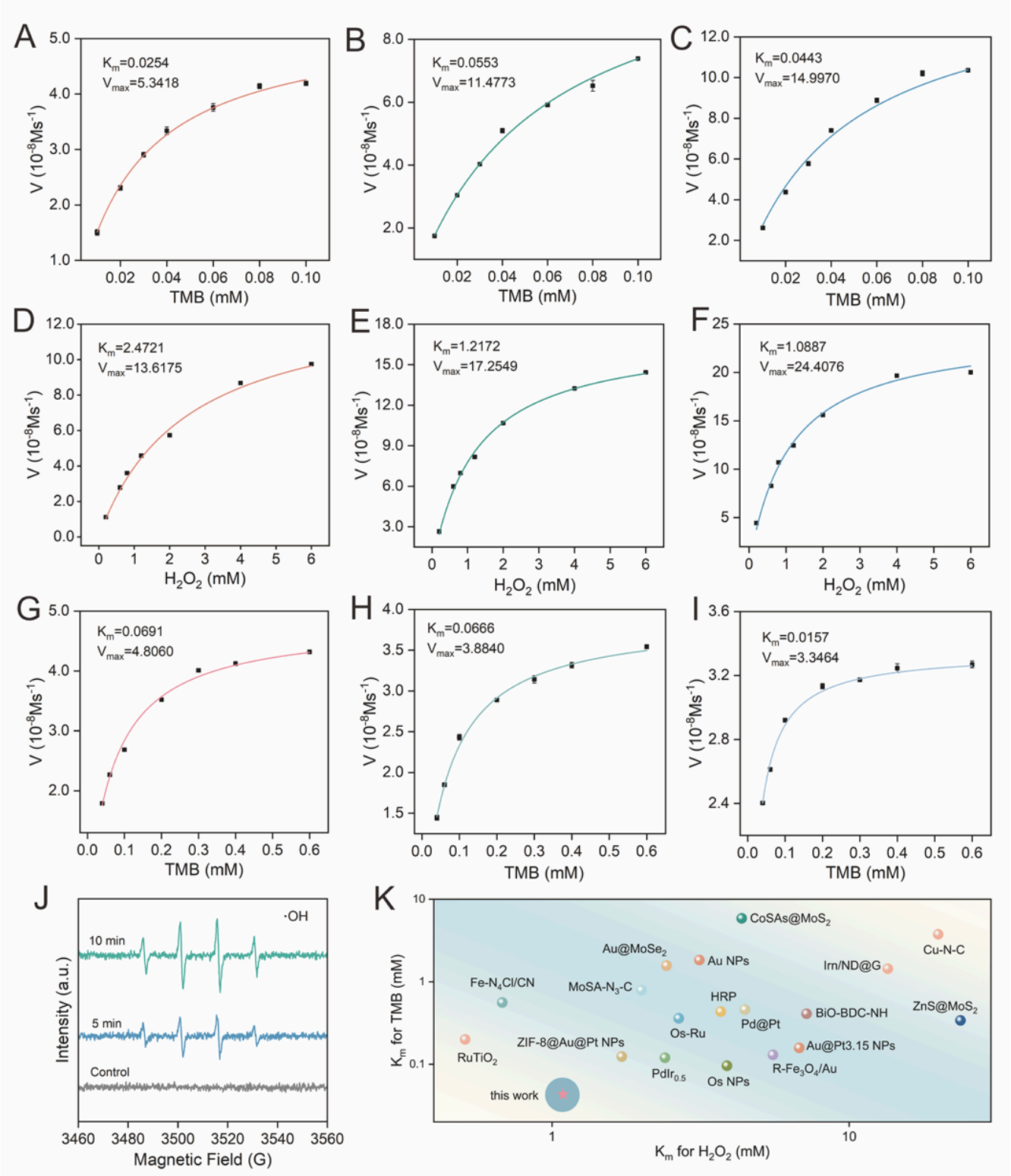

Figure 4

(A–C) POD-like kinetic curves of Au@Pd/Pt/PRTM, Au@Ir/Pt/PRTM, and Au@Ru/Pt/PRTM with TMB as the substrate. (D–F) Corresponding POD-like kinetic curves with H_2O_2 as the substrate. (G–I) OXD-like kinetic curves of the three nanozymes using TMB as the substrate. (J) Time-dependent EPR spectra confirming •OH generation in the Au@Ru/Pt/PRTM catalytic system. (K) Comparison of the apparent K_m values of Au@Ru/Pt/PRTM and representative reported nanozymes toward TMB and H_2O_2.

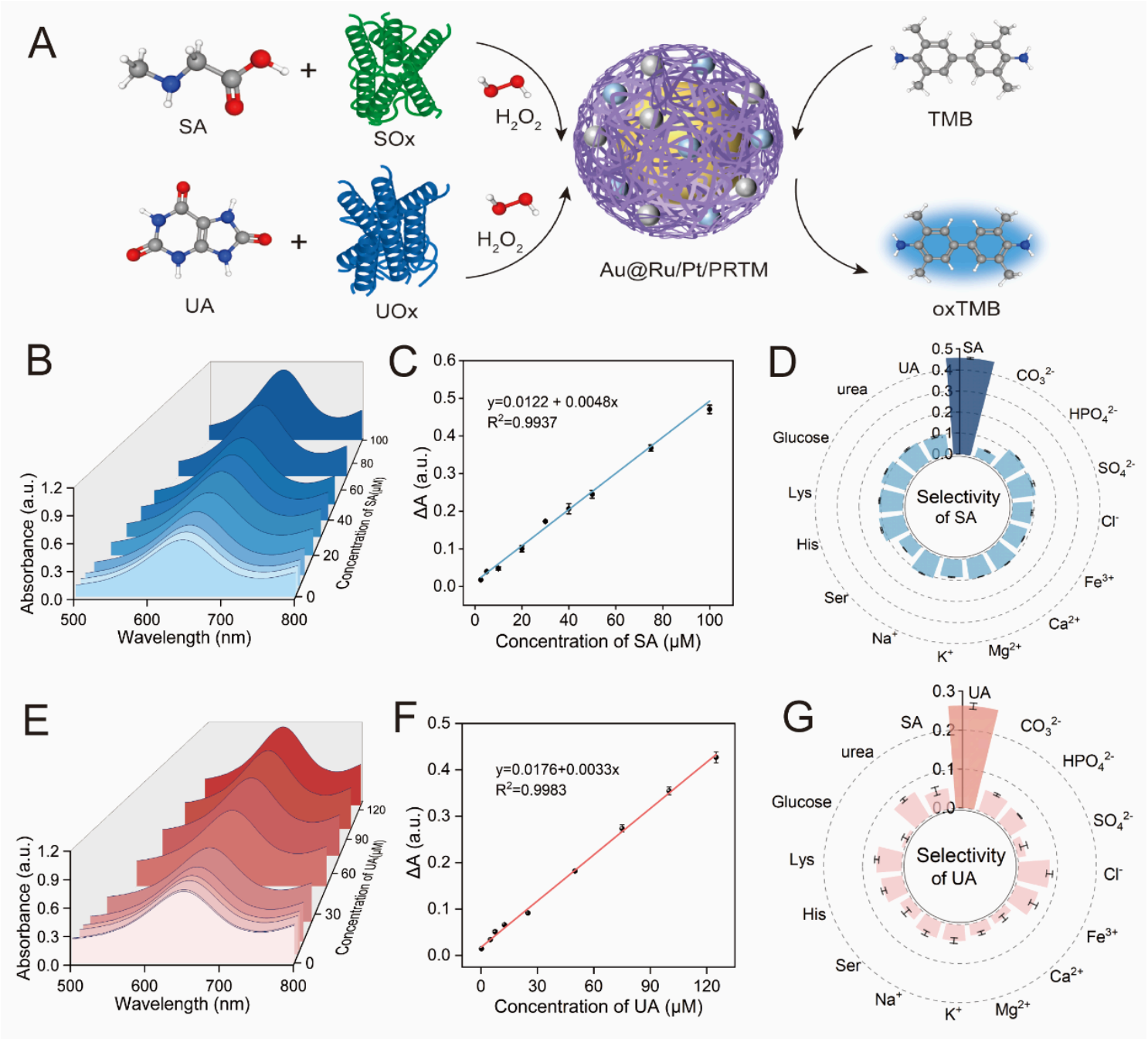

Figure 5

(A) Schematic illustration of the cascade colorimetric sensing mechanism. (B) UV–vis absorption spectra of the cascade colorimetric sensing system at different SA concentrations. (C) Calibration curve for SA detection. (D) Selectivity of the SA assay against potential interferents. (E) UV–vis absorption spectra of the cascade colorimetric sensing system at different UA concentrations. (F) Calibration curve for UA detection. (G) Selectivity of the UA assay against potential interferents.

Supplementary Files

This is a list of supplementary files associated with this preprint. Click to download.

- SupplementaryMaterial.docx
- Scheme1.png